New probes based on carbon nano-cones for scanning probe microscopies

Robin Cours, Germercy Paredes, Aurélien Masseboeuf, Thierry Ondarçuhu, Grégory Seine, Pascal Puech, Raul Arenal, Fabrice Piazza, Marc Monthioux

New probes based on carbon nano-cones for scanning probe microscopies

Robin Cours[a], Germercy Paredes[a,b,*], Aurélien Masseboeuf[a], Thierry Ondarçuhu[a,c], Grégory Seine[a], Pascal Puech[a], Raul Arenal[d,e,f], Fabrice Piazza[b], Marc Monthioux[a]

[a] *Centre d'Elaboration des Matériaux et d'Etudes Structurales (CEMES), UPR8011 CNRS, Université Toulouse 3, 31055, Toulouse, France.*

[b] *Laboratorio de Nanociencia,, Pontificia Universidad Católica Madre y Maestra, Santiago de Los Caballeros, Dominican Republic.*

[c] *Institut de Mécanique des Fluides de Toulouse (IMFT), CNRS, Université de Toulouse, Toulouse, France.*

[d] *Laboratorio de Microscopias Avanzadas (LMA), Universidad de Zaragoza, 50018 Zaragoza, Spain.*

[e] *Fundación ARAID, 50018 Zaragoza, Spain.*

[f] *Instituto de Nanociencia y Materiales de Aragon (INMA), CSIC-U. Zaragoza, 50009 Zaragoza, Spain.*

ABSTRACT

All-graphenic carbon morphologies grown on individual carbon nanotubes (CNTs) consisting of short-fiber segments bearing sharp micro-/nano-cones at both ends were mounted as new probes for scanning probe microscopies (SPM). Three mounting procedures were tested, two based on focused ion and/or electron beam processes operated in scanning electron microscopes, and another based on an irradiation-free procedure under an optical microscope. The benefits and drawbacks of all the methods are described in details. The extent to which the structural integrity of the carbon material of the cones was affected by each of the mounting processes was also investigated using Raman spectroscopy and high-resolution transmission electron microscopy. The carbon cones were found to be sensitive to both ion and electron irradiation to an unusual extent with respect to structurally-close nano-objects such as multi-wall CNTs. This was assumed to be due to the occurrence of a large number of free graphene-edges at the cone surface. The suitability of such carbon cones as SPM probes is demonstrated, the characteristics of which make them potentially superior to Si-, diamond-, or CNT-probes.

* Corresponding Authors.
E-mail addresses: gd.paredes@ce.pucmm.edu.do (G. Paredes); marc.monthioux@cemes.fr (M. Monthioux)

Keywords: carbon cone, graphene, scanning probe microscopy, focused ion beam processes, micromanipulator, irradiation damages.

1. Introduction

Scanning Probe Microscopy (SPM) is one of the most important characterization tools in material science for the last two decades [1]. It corresponds to a wide and still growing family of techniques based on the pioneering work carried out by G. Binning and H. Rohrer in the 80's, allowing to map the surface topography, to analyze the structure, and to measure the material properties at the nanoscale by using a scanning probe. In spite of their respective specificities, SPM modes share the need of a probe able to detect atomic-scale interactions. The probe characteristics determine the resolution, the analytical scope of the SPM [1,2], as well as the possible imaging artifacts. Therefore, developing new probes with, *e.g.*, improved resolution, better wear resistance and durability, low chemical reactivity, high aspect ratio, less sensitivity to undesired interactions with the probed material or others (e.g., adsorbed water), and better electrical conductivity (for conducting modes), remains a recurrent challenge [2].

SPM probes consist basically of a cantilever equipped with a tip at one end, the other end being attached to a sub-millimeter-large chip which allows the probe to be handled and secure in the microscope probe holder. Tip-sample interactions are then measured either by a direct determination of the cantilever deflection by a laser in the case of a contact mode, or by monitoring the amplitude or vibration frequency changes of the cantilever in so-called tapping mode during which the cantilever is put in oscillation. For this reason, cantilevers are, most of the time, metal-coated to enhance the back-surface reflectivity for the laser. Cantilevers are defined by their geometry such as length, width, thickness and mechanical properties such as the constant force (otherwise named "spring constant") and resonance frequency. The constant force and resonance frequency parameters are adjusted to the material and SPM mode requirements, but also define the quality factor and hence, the range of sensitivity allowed during the measurement [2]. On the other hand, the probe tip is defined by several parameters related to its dimensions: its apex radius or apex half-angle, length, and the so-called aspect ratio corresponding to the ratio of the tip length over the apex radius. The chemical nature, *i.e.*, the type of material which the probe is made of can also be an important parameter in some cases, although a vast majority is made of silicon, possibly doped to make it electrically conductive, or possibly functionalized for other SPM techniques such as chemical force microscopy [3].

The most cost-effective fabrication processes of SPM probes use a top-down approach based on lithography processes, which allow a scaled-up and single-step integrated-fabrication as well as

excellent reproducibility. However, this is valid only for Si-based materials, and, for most of cantilevers on market, probes are pyramid-shaped, exhibiting a low aspect ratio and a relatively large apex radius (Fig. 1a1-a2).

As a matter of fact, one of the biggest challenges for a SPM technique such as Atomic Force Microscopy (AFM) is to obtain a reliable image of sample surfaces with high roughness and steep topography variations. For such a purpose, a tip with both a small apex radius and a high aspect ratio is necessary. For overcoming the limitations of lithography-based processes in this regard, post-lithography microscale processes can be applied onto primarily-formed tips, for instance electrochemical etching, in order to lower the tip apex radius (Figs. 1b1-b2), or focused ion beam etching, in order to increase the aspect ratio (Figs. 1c1-c2). However, as a ceramic material, silicon is brittle, which affects the probe durability (wear resistance, breaking event) as more as the tips are sharper [4,5]. Furthermore, even if silicon can behave as a conducting material thanks to doping, metal coating steps (*e.g.,* with gold) are needed to enhance the electrical conductance for several SPM conducting modes.

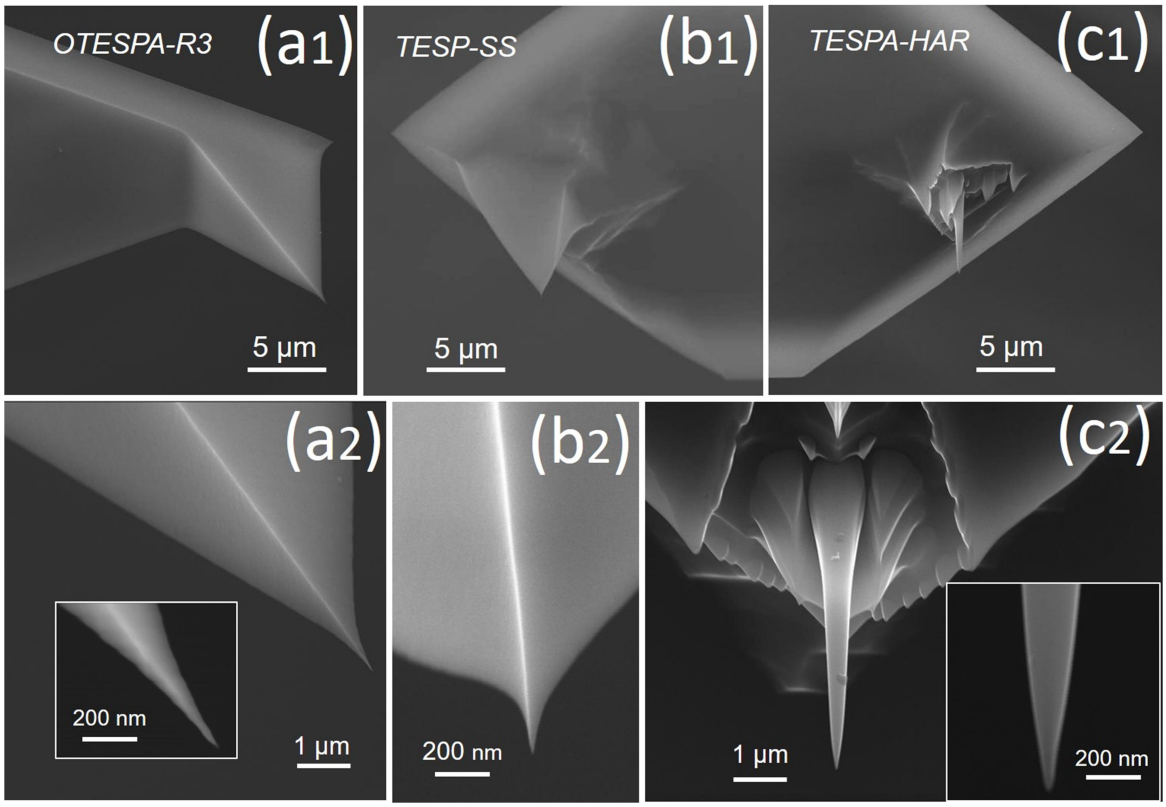

Fig. 1. SEM images showing the morphology and the apex of different silicon probes from the market. **(a1-a2)** A standard silicon probe of 7-10 nm apex radius (OTESPA-R3). **(b1-b2)** A "Super-sharp" Sb-doped silicon probe with a 2-5 nm apex radius, sharpened by electrochemical etching (TESP-SS). **(c1-c2)** A "high-aspect-ratio" Sb-doped silicon probe with a 10-15 nm apex radius, sharpened by ion milling (TESPA-HAR).

More recently, a bottom-up approach was also considered, for taking benefits of low dimensional objects presumably exhibiting the appropriate characteristics for being excellent SPM tips in their as-prepared form, such as carbon nanotubes (CNTs) [4-10]. CNTs exhibit excellent physical properties indeed: high mechanical strength and Young modulus [11,12], good wear resistance [5,6,9], and good electrical conductivity [6]. Diamond tips are also used for specific modes [13], but they exhibit two major drawbacks, namely mechanical brittleness and very low electrical conductivity. The bottom-up approach then mostly consists in either growing such a single CNT or diamond rod or cone at the suitable place on the cantilever, or growing it apart and then fixing it in a way or another at the right place, usually the apex of a silicon tip [4-10]. Both are quite difficult to achieve in a reproducible and robust way, specifically for CNTs as they are few-nanometer large individual objects. Therefore, either controlling accurately the growth direction or handling and positioning the tip is highly challenging (Fig. 2).

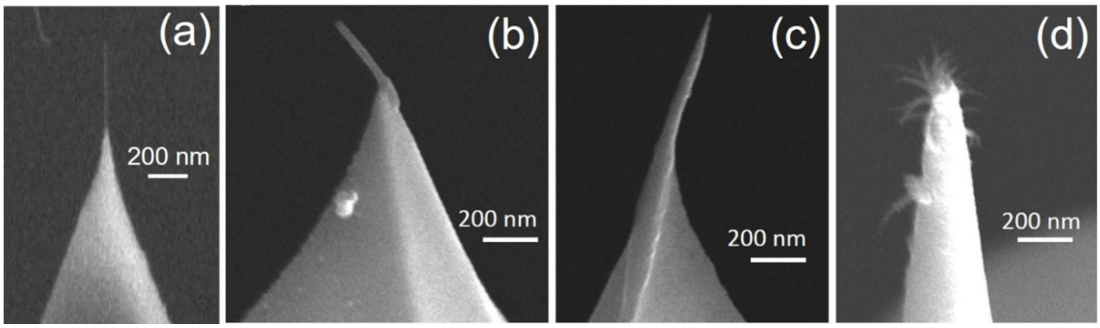

Fig. 2. SEM images of carbon probes obtained by bottom-up techniques. **(a)** A 300 nm-long CNT tip obtained by an in-SEM electron beam-assisted process, consisting of, first, welding the CNT onto an AFM tip by the electron beam-promoted deposition of amorphous carbon, and then shortening it by the focused electron beam [14]. **(b)** to **(d)** Commercial probes: **(b)** high-resolution carbon nanotube tip coated with a polymer for enhancing rigidity from CDI company; **(c)** from NanoScience company (no longer on market); **(d)** Diamond-like carbon probe from NT-MDT company. All show poor alignment, except in (a), but the positioning procedure makes the alignment poorly controlled anyway, and a perpendicular view would be needed to ascertain that the alignment is correct.

In addition, the relative flexibility of CNTs may generate imaging artifacts [15], compared to conical or pyramidal shapes. Generally speaking, a trade-off on the tip length must be found: a short length will limit the analysis of deep roughness, whereas a long length will impact the mechanical rigidity of the tip (hence likely to generate breaking, deformations, thermal vibrations, sensitivity to electrostatic forces, etc.). This trade-off is strongly dependent on the tip material. According to [16] for a cylindrical tip such as a CNT, a length in the range 0.5-1 μm is suitable in order to reduce excessive lateral flexibility and related image artifacts.

In this paper, we report the fabrication of a new type of SPM probes based on unique carbon cone-bearing graphenic micro-objects [17,18]. Many examples of carbon cones have been already reported in the literature (see Chapter 1 in [19]) but only few exhibit similar texture, nanotexture, and structure as ours, and none, as opposed to ours, are part of an overall, complex carbon microsized object which makes the cones actually able to be manipulated, mounted, and used for applications. As a matter of fact, very few graphene-based carbon cones were tested as SPM probes in the literature [20-21], and their characterization was quite limited regarding the carbon cone structure and texture resulting from the probe processing. The carbon cones used in the following are expected to combine the valuable characteristics of CNTs (high aspect ratio, wear resistance, electrical conductivity) thanks to their graphenic nature and high-rank nanotexture [22,23], and the valuable characteristics of Si or diamond tips (mechanical stability) thanks to their conical morphology. In addition, their unique as-grown association with a micro-sized carbon support (Fig. 3) makes them much easier to manipulate than CNTs in view of a bottom-up fabrication principle. Such a combination offers promising perspectives for their use as probes for a variety of SPM modes.

2. Starting materials for fabricating the probes

Carbon cones were obtained using a Time-of-Flight CVD process starting from a feedstock of CH_4 and H_2. The synthesis procedure followed that reported in [17,19]. The carbon micro-/nano-cones actually consist of a complex morphology made of a rough-surface microfiber segment extended at both ends by sharp cones with smooth surface (Fig. 3), which is grown onto a single CNT as support (not visible in Fig. 3). This is an important detail to know, because the alignment of the cones with respect to the microfiber segment which wears them strongly depends on the straightness of the supporting CNT.

The microfiber segment length, in the range of 10-20 µm, will allow the object to be easily handled and positioned during the mounting process onto the cantilevers. The cone length L is in the range of 2-8 µm and the width W at the base can reach 0.7-1 µm. The apex is characterized by an angle noted 2α. As an example, considering W = 700 nm and L = 6 µm leads to a 2α value of ~7°, which makes the apex quite sharp. However, this way of measuring the apex angle is mostly indicative, as the cone angle may change along the cone (for instance, some exhibit a kind of double meniscus shape [24]). The whole object forms as such all at once, with no additional process of etching or machining of any kind. Details on the formation mechanisms can be found in [23-25].

In the following, the whole object will be designated as "CnC" (for Carbon nano-Cone).

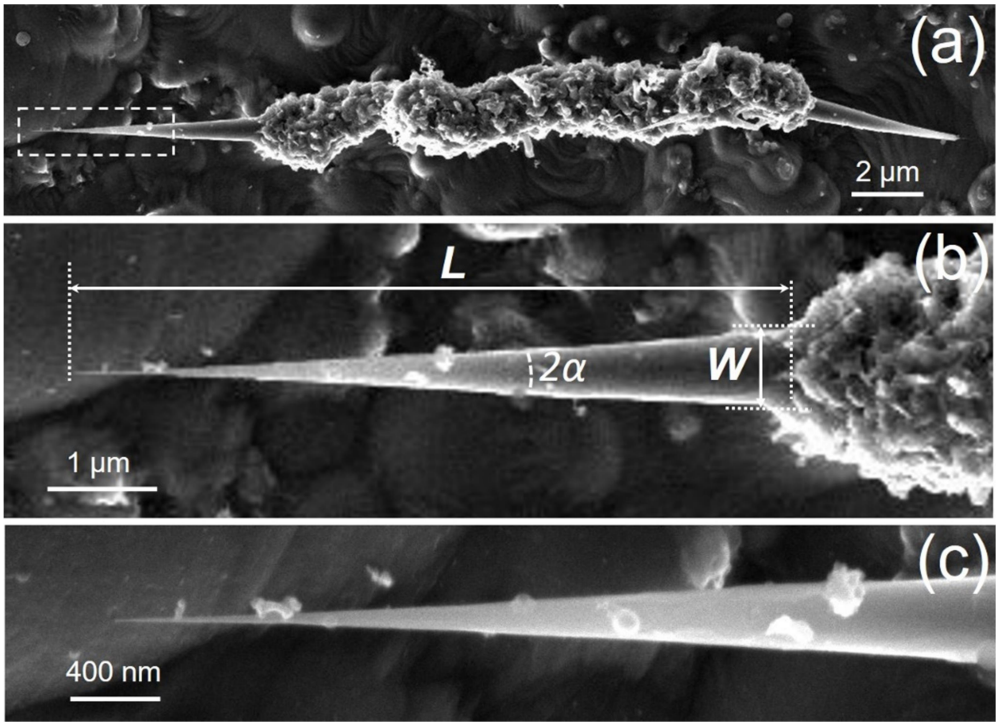

Fig. 3. From **(a)** to **(c)**, SEM images of a whole carbon micro-/nano-cone morphology (CnC) at increasing magnification. In (a), the framed area indicates the location of image (c); note that, if the left-hand cone is well-aligned with respect to the microfiber segment axis, the right-hand cone is not; such a misalignment is not rare in the current production, and can be worse than illustrated. In (b), geometrical characteristics with the length (*L*), width (*W*) and apex angle (2α).

The texture of the cones (*i.e.,* the arrangement of the graphenes within the cones) is similar to that of concentric-type multi-wall CNTs, although with the difference that the concentric graphene shells are turns of scrolls instead being individual graphene cylinders nested as in Russian dolls [23]. The graphenes involved are quite straight, suggesting that they are nearly defect-free (Fig. 4).

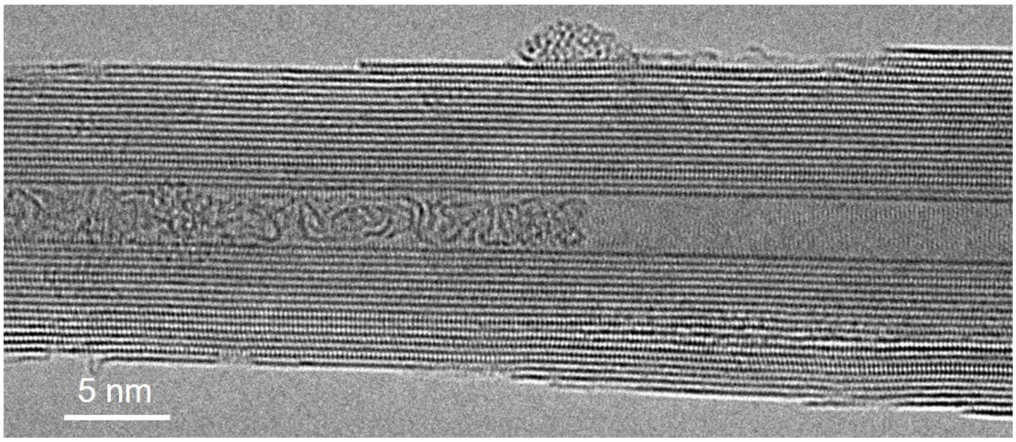

Fig. 4. High resolution transmission electron microscopy (HRTEM, aberration-corrected FEI TITAN Cube, 80 keV) image of a portion of a cone, showing the high-rank nanotexture, and the single-graphene steps responsible for the conical shape, and which provide the cone surface with atom-scale roughness.

Specific chip-supported tip-less cantilever beams ended by a cylindrical part of ~10 µm in height, carved out with a groove of few µm in both width and depth, were designed by us and then fabricated by AppNano (CA, USA) by lithography and then ion milling techniques (Fig. 5).

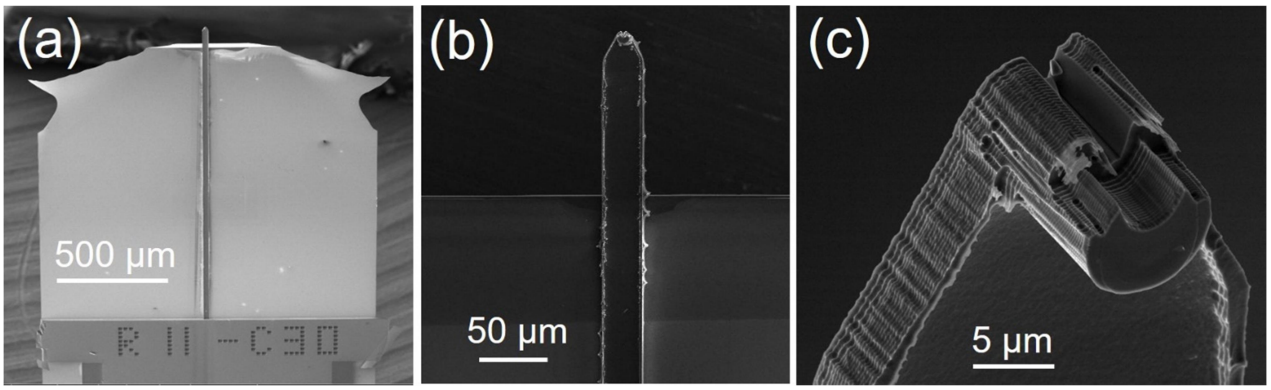

Fig. 5. Cantilever beams purposely designed at CEMES and then manufactured by AppNano company. **(a)** Overall view of the whole device, consisting in a cantilever beam supported by a chip, in this way strictly similar to that of regular AFM probes. **(b)** Closer view of the beam part. **(c)** Enlargement of the tip-less cantilever beam termination (Type1), showing the groove dedicated to receiving a CnC.

This design with a groove was intended to allow controlling both the orientation angle and the protruding length of the CnC during the mounting process. The cantilevers are made of silicon doped with antimony without any coating. The beam part is 115 µm in length and 35 µm in width. Two different cantilever batches were manufactured, the characteristics of which are gathered and compared in Table 1.

Table 1. Main characteristics of the two types of support-cantilever used in this work.

Sn-doped Si cantilever	**Type 1**	**Type 2**
Nominal thickeness (µm)	4.5 µm	0.5-1
Nominal spring constant (N/m)	40N/m	25N/m
Nominal Resonance frequency (kHz)	200-400	90-180
Quality factor (Q)	700-800	275
Electrical resistivity	00.1 – 0.025 Ω.cm	

3. Mounting processes

3.1. Gluing process

In this process, the assembling is conducted by means of a three-axis micromanipulator (from Micromanipulator, Inc.) under an optical microscope. CnCs are scrapped from their growth substrate so that they fall down onto a few-centimeter-large piece of silicon wafer, afterwards put under the optical microscope. Subsequently, a cantilever-chip is attached to the micromanipulator rod by using a tiny piece of adhesive film. Then, a small droplet of an ultraviolet (UV)-curable single-component optical adhesive resin (Norland NOA 68) is deposited onto a glass plate. A tiny quantity of resin is transferred by capillarity into the cantilever groove (Fig. 5c) by carefully touching the resin droplet surface with it using the micromanipulator. The resin transferred this way to the cantilever will allow retaining and attaching a CnC. Few minutes are needed to search, select, pick-up a well-aligned cone (with respect to the overall CnC axis) and grab it by the cantilever groove, thanks to the sticking force of the resin glue. The whole operation is monitored under a CCD camera visualizing the micromanipulator rod tip through the x100 objective lens of the optical microscope.

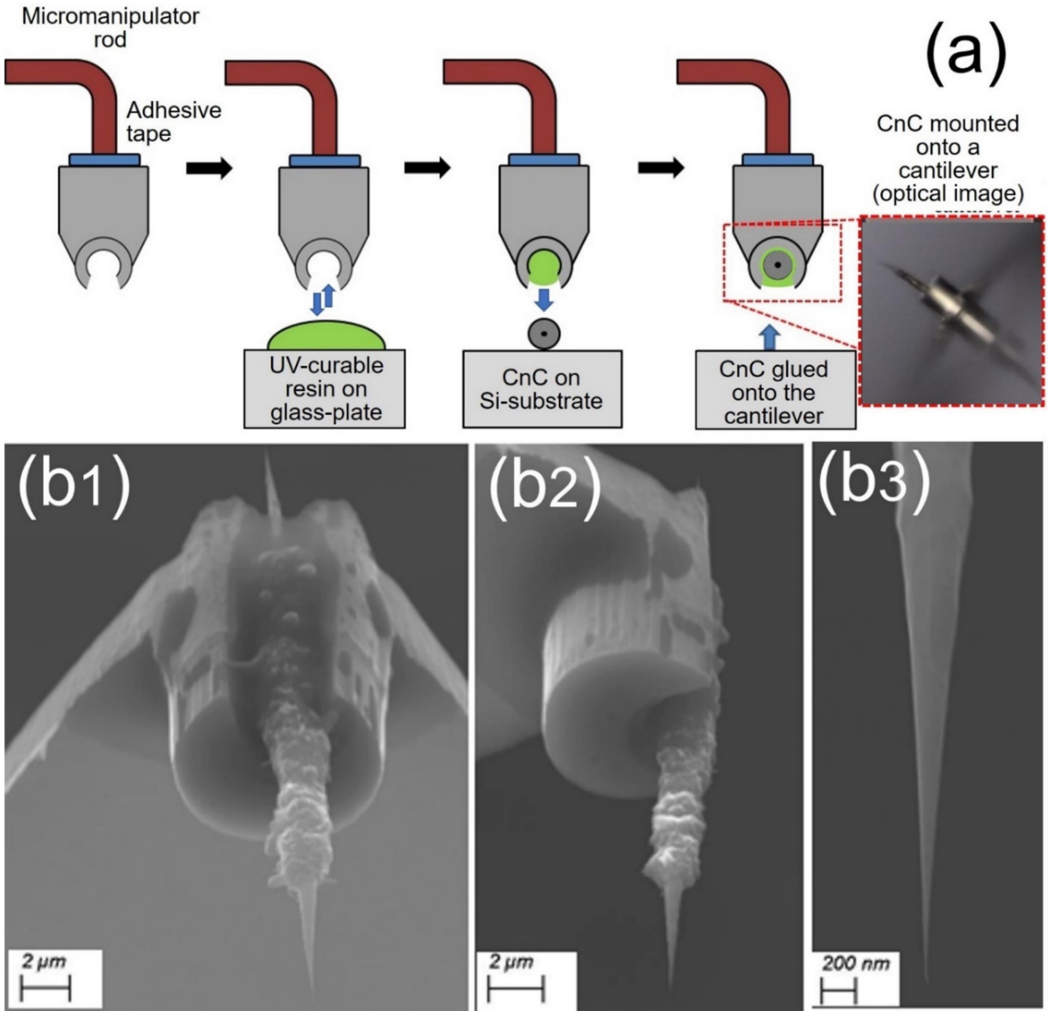

Fig. 6. (a) Sketch of the gluing mounting process of a CnC onto a cantilever. As a CnC always exhibits two cones, the one oriented towards the cantilever backside is useless. **(b1)** to **(b3)** SEM images of a carbon

probe right after the gluing mounting method. In this example, the cone is fairly well aligned with respect to both the short-fiber-part axis and the groove axis.

The resin is then cured under an ultraviolet lamp (12 W, specimen at ~5 cm distance, 2 hours with a 350-380 nm wavelength range). Such a wavelength is not in the adsorption range of CNTs [26], hence it is assumed that it is not harmful to the concentric graphenes making the cones either. The whole mounting process takes 15-20 min when performed by a trained operator. The mounting steps are sketched in Fig. 6. Finally, SEM characterization is conducted to verify the alignment and orientation of the cone tip with respect to the cantilever groove, as shown in Fig. 6. Since the UV resin employed is not electrically conductive, the probes made by this method can only be dedicated to non-conducting SPM modes.

The interest of the process is its speed, and the relatively low cost of the equipment involved. On the other hand, because of the limited magnification power of the optical microscope, the lack of 3D view, and the "capturing" effect of the CnC by the resin once both are put in contact, subsequently correcting any misalignment of the cone axis with respect to the cantilever, either intrinsic to the morphology selected or resulting from the picking-up and gluing step, is not possible. However, once getting trained with the procedure, only few (~10%) fabricated CnC probes revealed to be non-usable.

3.2. Welding processes

3.2.1. Fully or partly using focused ion beam (FIB)

A Thermo Fisher HELIOS NanoLab 600i FIB equipped with a rod-like micromanipulator (Omniprobe), and a gas injection system (GIS) was used. The GIS spreads organometallic precursor molecules (here, $(CH_3)_3Pt(CpCH_3)$ for platinum or $W(CO)_6$ for tungsten) that are decomposed and ionized by a focused beam of Ga ions. The metal atoms, released by the interaction of the precursor and the Ga ion beam, deposit on the part of the substrate onto which the Ga ion beam is focused. This is the principle of focused ion beam-induced deposition (FIBID). The focused Ga ion beam can also be used to cut and trim by etching specimen parts (FIB-etching). CnC probes were prepared by adapting an all-FIB-based procedure (FIBID + FIB-etching) previously developed for mounting a CnC as an electron emitter [27]. A CnC is selected from the growth substrate and then first welded to the micromanipulator rod by the FIBID of Pt or W (Fig. 7a). Then the CnC is moved until reaching the cantilever, placed in the cantilever groove (Fig. 7b), welded by FIBID again, and then released from the micromanipulator by removing the welding material by FIB-etching (Fig. 7c).

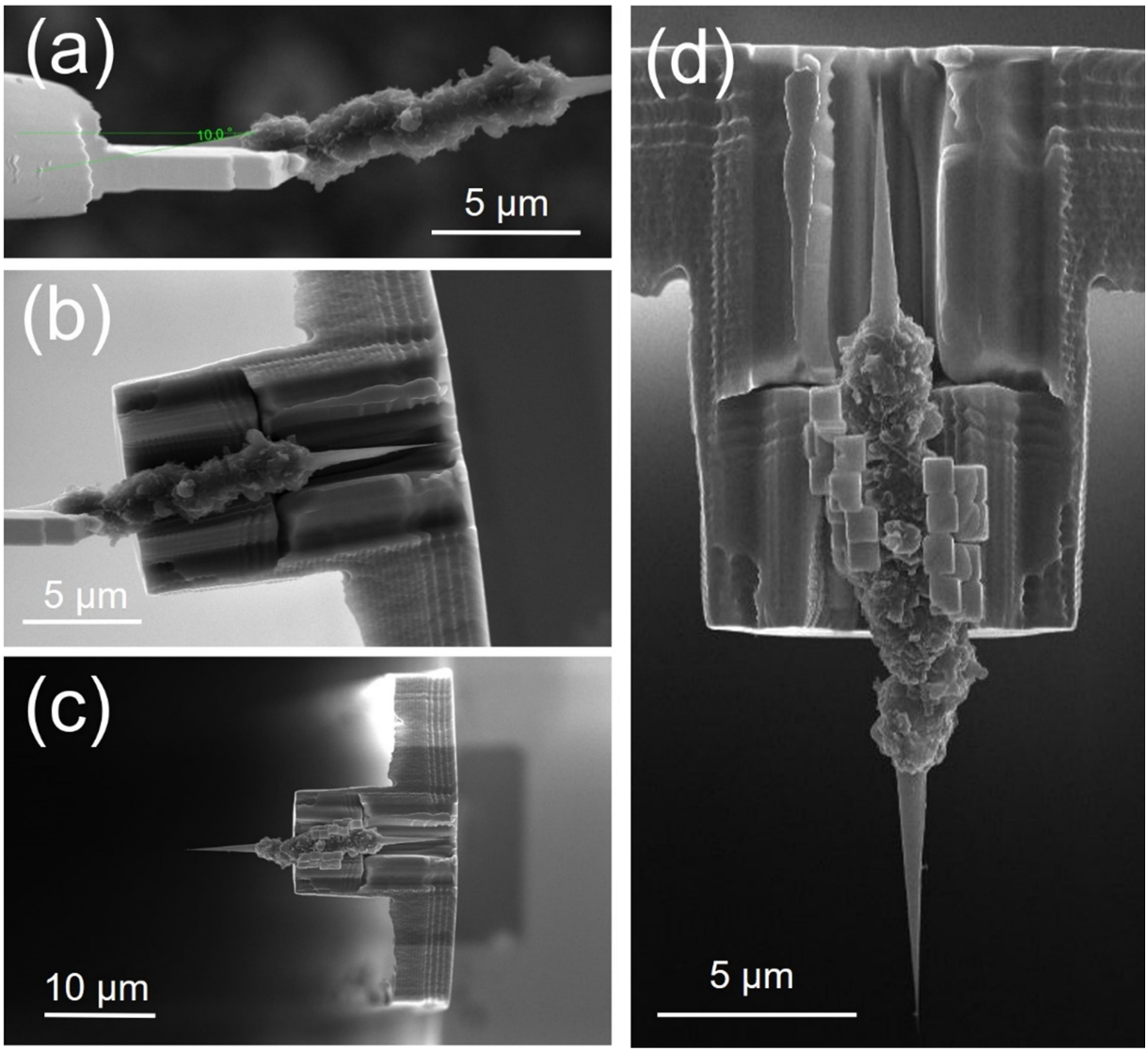

Fig. 7. Various steps of the mounting process using FIB. **(a)** the selected CnC is welded to the micromanipulator rod by FIBID. **(b)** The micromanipulator brings the CnC into the cantilever groove. **(c)** The CnC is welded to the cantilever by FIBID, and then released from the manipulator rod by FIB-etching. **(d)** enlarged view of (c) showing the CnC, the cantilever, and the welding material.

After several tries during which standard high currents were first used, we ended by using the same low currents for both the FIBID and FIB-etching steps, typically 7 pA at 30 keV, in order to avoid a visible alteration of the cone morphology due to irradiation damaging (see Sections 5.1 and 5.2). And then, to tentatively limit even further the damaging effect by ion irradiation, the first two FIBID steps were replaced by focused electron beam-induced deposition (FEBID) steps for which beam conditions were milder (2 keV, 170 pA and 2 keV 700 pA, for the rod/CnC welding step and the CnC/cantilever welding step, respectively). And finally, to limit even further the risk for irradiation damages, the mounting was finally made using FEBID only and no etching step, as described in Section 3.2.2.

Besides, although the deposited metal exhibits facetted shapes suggesting it is crystallized (Fig. 7d), it also contains a significant amount of carbon (from the precursor) which may affect the electrical conductivity. Therefore, W was finally preferred over Pt because the resulting electrical conductivity of the welding deposit is better [28].

3.2.2. Focused electron beam-induced deposition (FEBID)

The principle of FEBID is the same as for FIBID, except that a focused electron beam is used instead of a focused ion beam. A ZEISS 1540XB FIB Dual Beam was used, where the micromanipulator consists of microsized clamps (Fig. 8) that allow the CnC to be grabbed, moved, and then released merely by actioning the tweezers. Therefore, the electron beam (2 keV, 200 pA) is used only once, for welding the CnC to the cantilever groove, yet over long deposition times (several tens of minutes) in order to deposit enough W to secure the welding as far as possible.

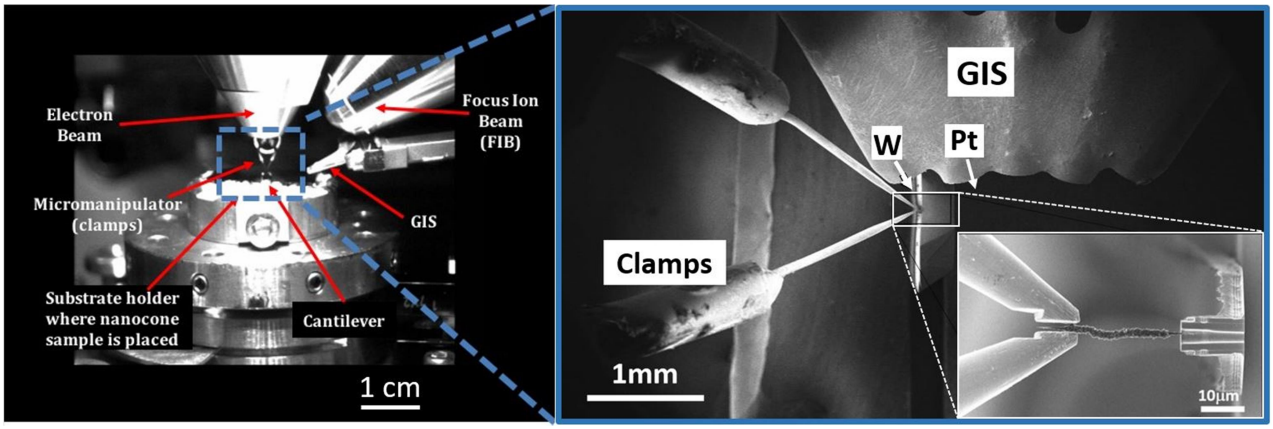

Fig. 8. Configuration of the ZEISS SEM equipped with a cross-beam system used for FEBID. The configuration for the Helios SEM is similar. The various insets on the right show details on the clamps and the spatial relationships between the clamps, the GIS, and the cantilever holder.

The benefit of using a micromanipulator equipped with clamps instead of a single rod is to limit the possible interactions of the CnC with the Ga ion beam, whereas such interactions occur 1-3 times with the procedure described in Section 3.2.1. Also, the tweezer branches can somewhat protect the CnC from the electron beam [29]. Indeed, because of the light weight of carbon atoms (Z = 6), specifically when compared to the heavy weight of Ga atoms (Z = 31), irradiation damaging can always be suspected, in spite of the strong C-C bond in graphene (~600 kJ/mole). For the same reason, using electrons as in FEBID instead of heavy ions as in FIBID is also supposed to lower dramatically the effect of irradiation damaging. The drawback is that the metal deposition rate is lower. This is not a major issue when the object to weld is nanosized, such as CNTs [30], but it is more an issue for much larger objects such as ours. It could make possible the

attachment to be loose (Fig. 9), resulting in a non-standard behavior, imaging artifacts, or even the subsequent loss of the CnC during the resonance frequency measurement step or in operation.

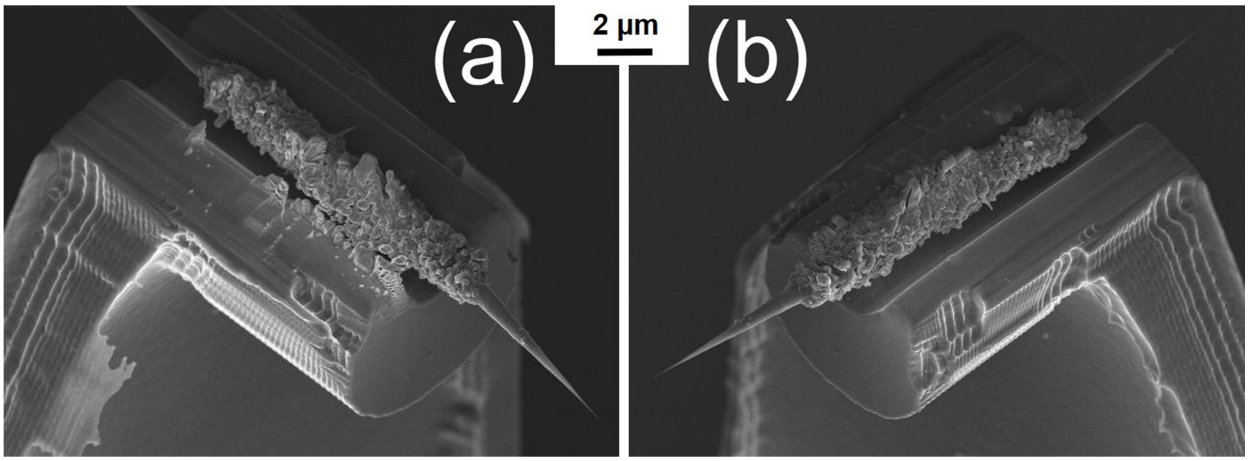

Fig. 9. Example of a FIBID-prepared CnC-probe showing a probably-loose attachment with **(a)** poorly adhering welding material on one side, and **(b)** no welding material on the other side.

The whole mounting procedure using FIBID or FEBID welding techniques takes about 3 hours from the time the CnC is being selected onto the growth substrate to the time a probe is ready (slightly shorter processing times are possible when using the Omniprobe micromanipulator, the use of which is less tricky than that of the clamp micromanipulator). The expected advantage of the welding techniques was that the resulting probes could be used for both non-conducting and conducting SPM modes.

4. Characterizing the probes

4.1. Resonance frequency

The effect of the mass added to the cantilever by welding a CnC was evaluated by measuring the resonance frequency of the cantilever with and without a CnC mounted. The effect appeared to be tiny, in the range of a 2 kHz downshift (Fig. 10a) with respect to the nominal values (in the range of 250-350 kHz for Type1 cantilevers and 90-180 kHz for Type2 cantilevers), rising the question whether such a slight change was significant or not.

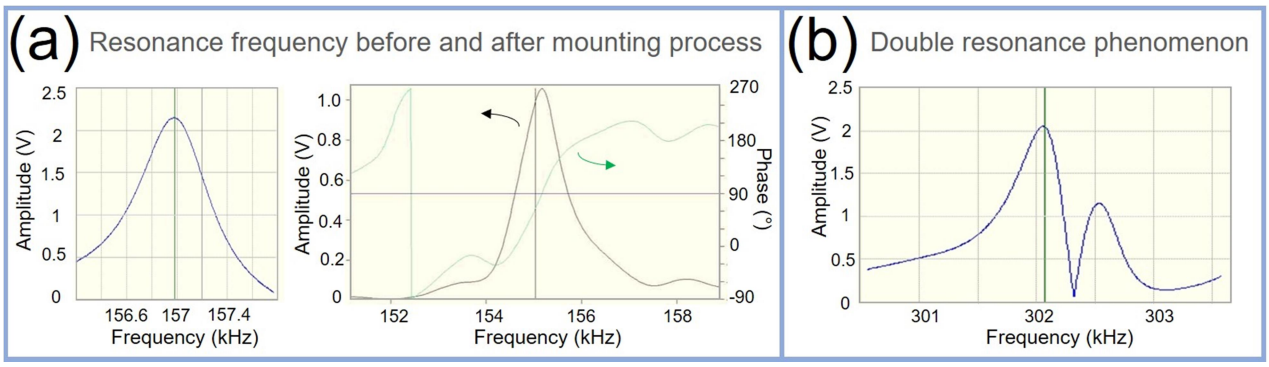

Fig. 10. (a) Example of cantilever resonance frequency recorded before (left) and after (right) mounting a CnC. **(b)** Example of a double resonance phenomenon evidenced sometimes after mounting a CnC.

In order to figure out, the weight of a typical carbon morphology such as shown in Fig. 3a was estimated, considering it to be made of a cylinder (with length L_f = 15 µm and radius r_f = 1 µm) added with two cones (with L_c = 5 µm and base radius r_c = 0.4 µm). As the fibrous part with rough surface (*i.e.*, the cylinder) is porous with the average pore width in the range of few nm [22], we gave to it a density similar to that of glassy carbons, *i.e.*, 1400 kg/m^3. As the cone parts are dense, made of perfect graphenes, highly packed as in graphite, but with mostly a turbostratic structure [23] (which means that the intergraphene distance is ~0.34 nm instead of 0.335 nm as in genuine graphite), we gave to them a density slightly lower than that of graphite, *i.e.*, 2000 kg/m^3. As a result, the total calculated weight is ~69 pg.

On the other hand, by applying principles similar to that developed in papers such as [31,32], we deduced the weight added to the cantilever tip so that it induces a 2 kHz downshift of the resonance frequency. As a result, the calculated weight is ~67 pg.

Therefore, yet of a small extent, the change in the resonance frequency of the cantilevers after being attached a carbon morphology at their tip is definitely significant and can be used to estimate the weight of the carbon object added [31,32]. The detail of the calculations is provided as **Supplementary Information**.

An experimental feature of the resonance curves, which was observed several times for the CnC probes but was unusual for regular Si probes, is the occurrence of an effect of resonance oscillation as a double peak (Fig. 10b). This could be a consequence of a loose mounting as discussed at the end of the previous section.

4.2. Tip alignment and geometry

For analyzing surfaces with large topography variations, the alignment of the tip axis (here the cone axis) with respect to the symmetry plane of the cantilever (the one which contains the groove

axis in our cantilevers) should be known and, if possible, should be the same for each probe. This alignment can be defined by two deviation angles, *i.e.,* the out-of-plane angle θ and the in-plane angle φ between the cone axis and the groove axis, as depicted in Fig. 11.

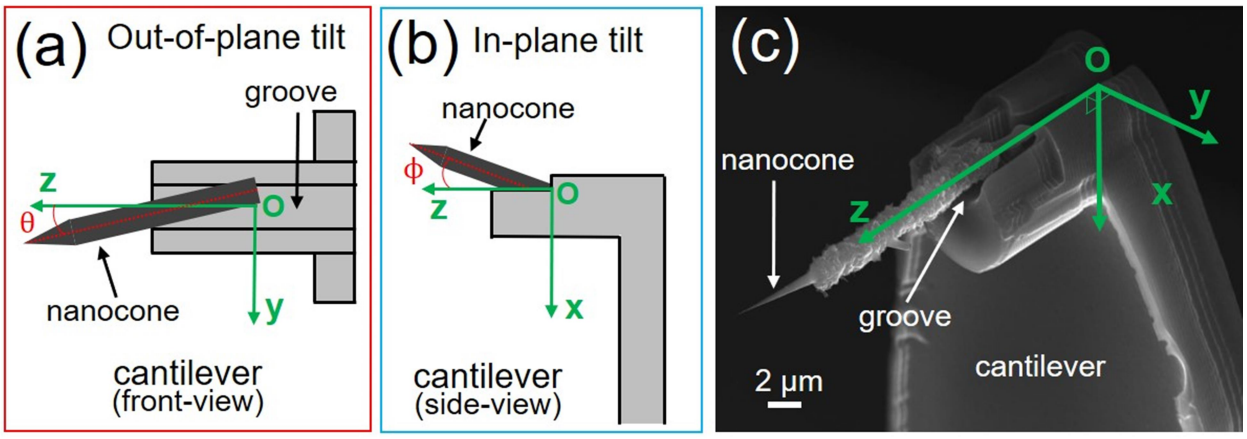

Fig. 11. Sketch of the geometric angles of interest using the example of a CnC probe. **(a)** Front view; θ is the out-of-plane deviation angle (with the reference plane being the symmetry plane (x,z) of the cantilever, which contains the groove axis). **(b)** Side view; φ corresponds to the in-plane deviation angle formed by the cone morphology axis and the Z axis. **(c)** The various axes reported onto a real probe.

To achieve the best imaging performances, θ should be as low as possible, tending to zero, while φ should ideally tend to 11-13° in order to compensate the standard tilt angle of the cantilever holder. A SEM control of ~130 CnC probes fabricated using either the gluing or the welding processes showed a large variability of these angles (Fig. 12), both due to *(i)* the lack of accurate positioning of the CNC into the cantilever groove, and to *(ii)* the variability of the CnC morphology for which the cones are not always well-aligned with respect to the short microfiber segment wearing them (Fig. 3, and related comments).

Because of the chances for more or less severe probe tip misalignments, this first-generation CnC probes are poorly suitable for analyzing substrates with high amplitude of abrupt topography variations, unless special care is taken with selecting well-aligned ones through SEM investigation. However, this limitation will be able to be overcome by growing CnC onto perfectly straight CNTs. This *(i)* would fix the problem of cone axis versus fiber segment axis misalignment, and *(ii)* could dramatically lower the risk of misalignment during the mounting. The literature shows examples of such isolated, perfectly straight, and parallelly-aligned free-standing CNTs [33].

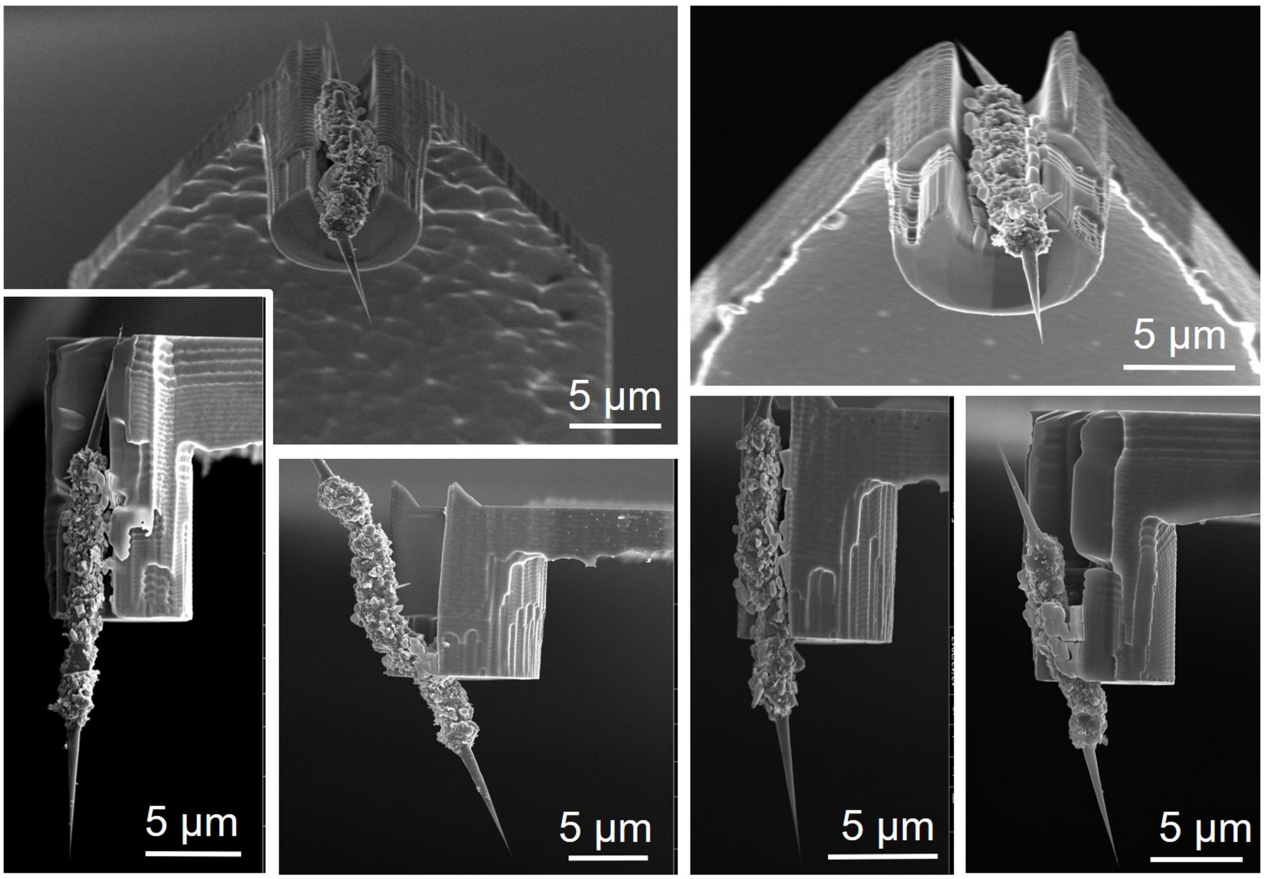

Fig. 12. SEM images showing various examples of as-prepared CnC probes showing more or less severe deviations of the θ and/or φ angles with respect to standards.

5. Characterizing the carbon from the probes

5.1. Morphology analyzis by SEM

As said previously, carbon-based materials are likely to be sensitive to irradiation damages, that welding techniques were suspected to generate. Although SEM is not able to discriminate whether a material is crystallized or amorphous, cones from CnC were shown to exhibit morphological changes (buckling) in the vicinity of the apex after welding, specifically when using FIBID, suggesting that some structural change happened. Fig. 13 confirms that the morphological change after the FIBID procedure is actually due to the interaction with the focused Ga ion beam because it did not happen – with very seldom exceptions - when using the ion-free mounting procedure described in Section 3.2.2, and never happened when using the gluing procedure. Furthermore, it seems that the tip buckling is proportional to the total ion dose received (*i.e.*, the number of ions received over the cumulated exposure times), although this statement could not be otherwise than qualitative. Indeed, a CnC extensively welded onto a Cu substrate aiming at preparing a cross section by FIB ablation exhibited the largest deformation of all (Fig.

13a), followed by a CnC mounted as a probe using an all-FIB procedure (*i.e.*, FIBID + FIB-etching, Fig. 13b), to be compared to Figs. 13d-f where a combined FEBID + FIB-etching procedure was used.

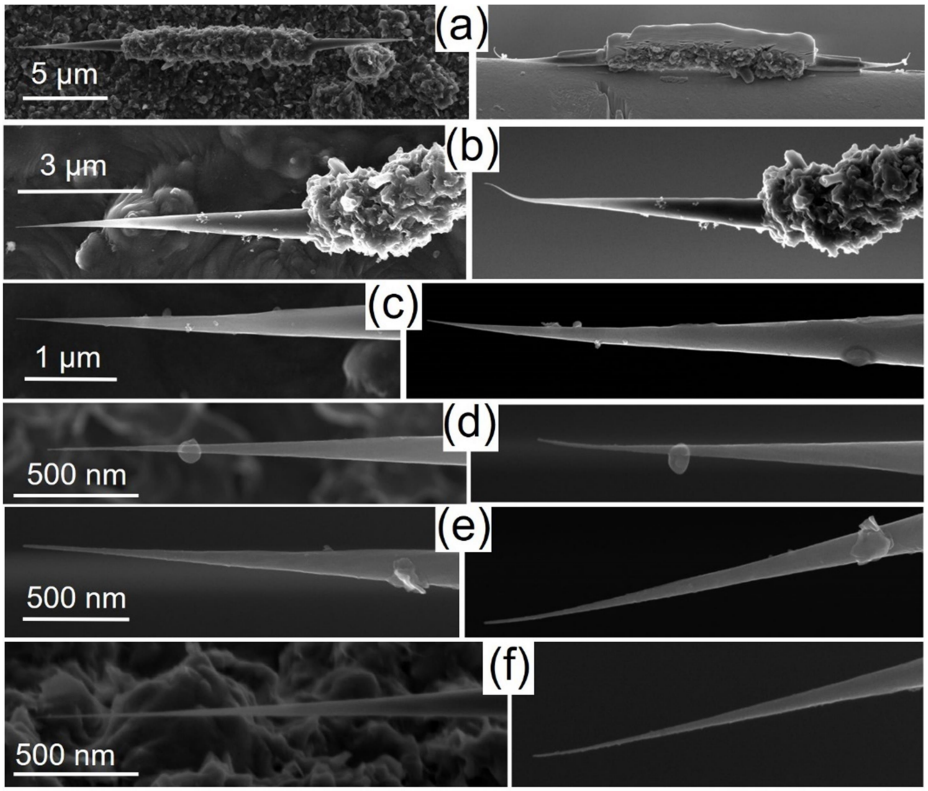

Fig. 13. From **(a)** to **(f)**: Examples of decreasing buckling induced to the cone tip of CnCs due to the presumably decreasing effect of the focused beams during the welding and/or etching steps. Left images: as-prepared CnC, on the growth substrate, before any contact with focused beams. Right images: the same, after welding onto a cantilever. **(a)** morphology selected and then extensively welded by FIBID onto a Cu support prior to preparing a longitudinal cross-section of it by FIB-etching. **(b)** and **(c)**: CnCs mounted as probes using both FIBID and FIB-etching. **(d)** to **(f)**: CnCs mounted as probes using FEBID combined with FIB-etching.

5.2. Raman spectroscopy

Raman spectroscopy is a common analyzis technique to investigate the structure and nanotexture of graphenic carbons, in particular through the measurement of the intensity ratios of the D band (which reveals the occurrence of various types of defects) over the G band (which is associated with the perfect graphene lattice, as the 2D band is) [34]. A Jobin-Yvon Horiba, Labram HR EVO Raman spectrometer was used, coupled to an AFM plateform TRIOS, with the following conditions: laser λ of 632.8 nm, laser spot size of 0.5 µm, power of 0.7 mW, exposure time of 200 s. In order to record the D, G and 2D bands at the same time, a 76x76 mm grating with

600 gr/mm was used to get the spectral range required. Raman spectra were then obtained on CnC probes to evaluate the effect of each of the mounting techniques (*i.e.*, gluing, FEBID, FIBID) on the final structural quality of the probes (Fig. 14). For this, the CnC probes were mounted on the holder and characterized locally thanks to the nano-positionning facilities. Raman maps were obtained in the XY plane and in the XZ plane with an integration time of 10 s. The spatial step is 200 nm. By interpolation, the location of the tip was determined with an accuracy of about 100 nm. Long acquisition times in different places were possible due to mechanical stability. In this set of experiments, the laser probe was focused far from the apex, on the junction between the fiber segment and the cone base, thereby partly overlapping both, so that the Raman laser will probe about the same volume of carbon material for each probe, as far as possible.

As the carbon tip is in air, there is no electric field enhancement by substrate effect. Consequently, no heating effect was observed. This is ascertained by the stability of the amorphous carbon part under the laser beam: upon a time increase from 10 to 200 s, no modification of the Raman band shapes was observed.

Fig. 14 shows significant differences between the CnC welded by FIBID (bottom spectrum), that welded by FEBID (middle spectrum), and that merely glued by the UV-cured resin, hence not subjected to any ion or electron irradiation step (top spectrum).

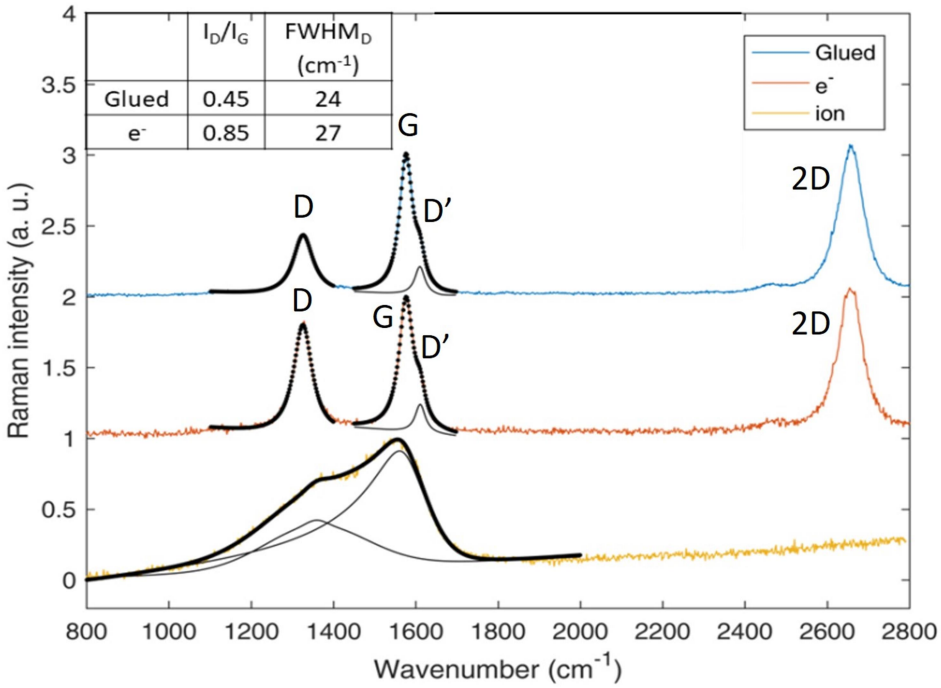

Fig. 14. Raman spectra (with the fitting as the black solid and dotted heavy lines) recorded on the cone/short-fiber junction of three different CnC probes mounted by the three different procedures described in Section 3: **top** (blue spectrum): glued with a UV-cured resin; **middle** (red spectrum): Pt deposited by FEBID; **bottom** (yellow spectrum): Pt deposited by FIBID and then release of the Omniprobe by FIB-etching. In the top-left part of the Table are provided the I_D/I_G band intensity ratio as well as the linewidths

of the D band for the glued or the FEBID-mounted CnC only. These parameters could not be calculated for the FIBID-mounted CnC since the related spectrum (bottom) no longer exhibits the regular D + G + 2D bands typical of graphenic carbon materials.

The I_D/I_G ratio (0.45) of the gluing-mounted CnC probe may serve as reference, as the related CnC was never subjected to any electron or ion irradiation. For the FEBID-mounted CnC (middle), the graphenic nature is obviously maintained as the G and 2D band intensities remain unchanged, as well as the G band linewidth (~20 cm^{-1}), but an increase of defects is observed as revealed by the significant increase of I_D/I_G (from 0.45 up to 0.85) and a slight increase of the D band width (from 24 to 27 cm^{-1}). According to Cançado *et al.* [35], this reveals a concentration increase of point-defects (*e.g.*, interstitial atoms, substitutional atoms, vacancies) preferably to line defects (*e.g.*, screw or edge dislocations, grain boundaries), which is consistent with an effect of irradiation damages. Finally, the spectrum for the FIBID-mounted CnC (bottom) shows a dramatic change and is now typical of amorphous carbon, where the D and G bands merge to form a broad band, and where the 2D band is no longer observed.

Considering that 87% of the Raman signal comes from a depth $d = \lambda/(4\ \pi.\kappa)$, where λ is the incoming wavelength (here, 632.8 nm), and κ is the extinction coefficient which depends on the wavelength, the estimated laser probe penetration ranges from ~40 nm if the material is graphenic carbon (for which κ ~1.35 [36]) to ~80 nm is the material is amorphous carbon (taking κ ~0.8 as a plausible value [37]).Therefore, the spectra obtained are mostly representative of the surface state over few tens of nanometers, not of the bulk. Only the use of focused Ga ions (FIBID) heavily amorphizes the carbon material surface, whereas the use of focused electrons (FEBID) mostly increases the surface concentration of defects.

5.3. Transmission electron microscopy

The cone apices of as-prepared CnCs were investigated by HRTEM (FEI Titan Cube, aberration-corrected TEM equipped with a Schottky electron source and operated at 80 kV). Two examples are shown in Fig. 15. A comprehensive study of them can be found in [23]. HRTEM imaging allows roughly estimating the apex radii R1 and R2 of the cone tips at 2.2 and 3 nm, respectively, making expect that CnC probes will be able of high resolution when used in AFM mode. Moreover, depending on the surface characteristics to be investigated (for instance, a surface with a roughness below 1 nm) smaller morphological features of the apex surface other than the overall cone shape may prevail in the interaction with the substrate, such as the protruding detail arrowed in Fig. 15a, which may provide the probe with even higher resolution, as such an apex is likely to be efficient in revealing atom-scale details in roughness-free substrate.

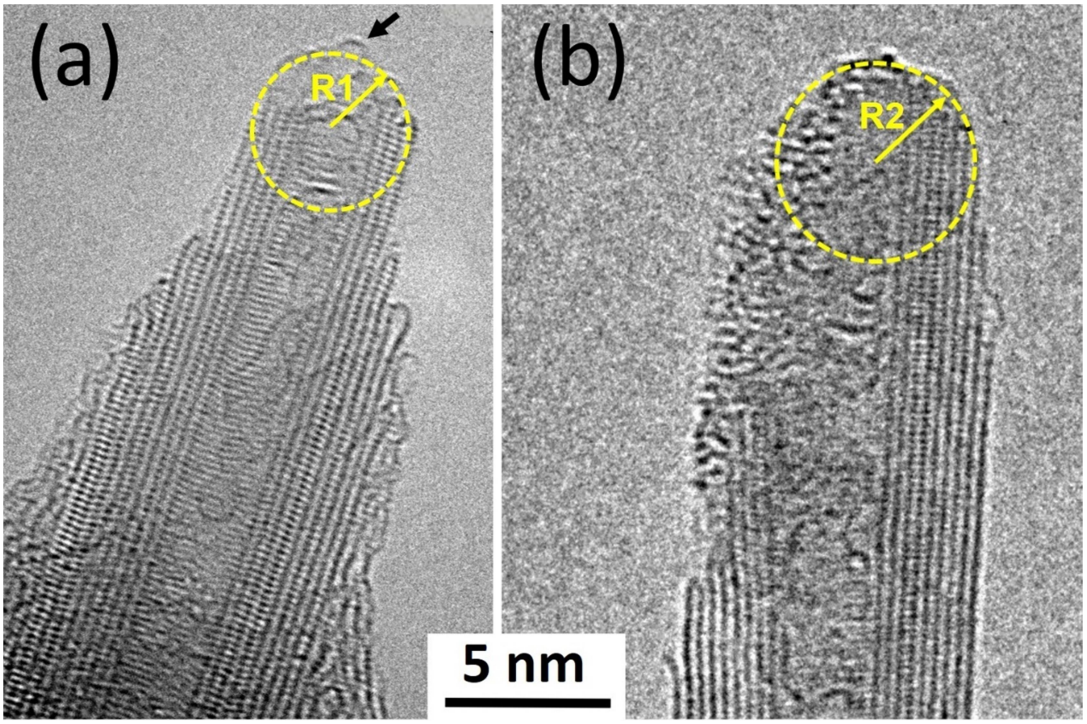

Fig. 15. (a) and **(b)** HRTEM images (80 keV) of two cone apices from as-prepared CnCs. Modified from [23].

In order to check the extent of the irradiation damages evidenced by the Raman investigation (see Fig. 14 and related comments), FIBID-mounted CnC probes were investigated by HRTEM. A special TEM specimen holder was purposely modified by us so that a whole CnC probe could be put into the TEM (Fig. 16a). In order to serve as dimensional reference, the HRTEM image of the as-prepared cone apex provided as Fig. 15a is reproduced here as Fig. 16b. The structural integrity of the tips appeared to be systematically affected for the FIBID-mounted CnC probes (Figs. 16c-f), but also, surprisingly, for a gluing-mounted CnC probe (Fig. 16g). This apparent contradiction with what was expected from the gluing mounting process (which does not include any electron or ion irradiation step) and from the Raman results requires a closer look.

An extensive yet variable degree of amorphization of the carbon material over lengths of several hundred nanometers up to 1-2 micrometers away from the apex, and a dramatic increase of the apex radius of the tip were observed for all the FIBID-mounted CnC probes investigated (Figs. 16c-f). Rapidly, for cone diameters above ~100 nm, it cannot be said whether the amorphization affects the bulk or only the cone surface, and if so, how deep, because of the 2D-projection effect and the penetration limit of the electron beam. In some cases (Fig. 16d), the amorphization of the cone tip appears to be surface only, but we must remember that what is seen is only what remains from the tip. The dramatic increase of the tip radius systematically observed is then mostly due to the shortening of the cone because of the loss of the thinnest portion of the cone end, added to a

swelling effect resulting from the structure change (from graphenic turbostratic to amorphous). This is somehow consistent with the literature, as FIBID Pt deposition was acknowledged to provoke higher disorder and impurity content than FEBID by the presence of a higher concentration of Pt grains in the material as well as possible Ga ion implantation [38]. Furthermore, a heavy ion beam was found to be able to break C-C bonds and change the structural properties of graphenic carbon materials [39,40]. For instance, the amorphization of MWCNTs, which are structurally close to our carbon cones, was reported by using Ar ions (with an irradiation dose of $4x10^{16}$ ions/cm^2) at an energy as low as 3 keV [40].

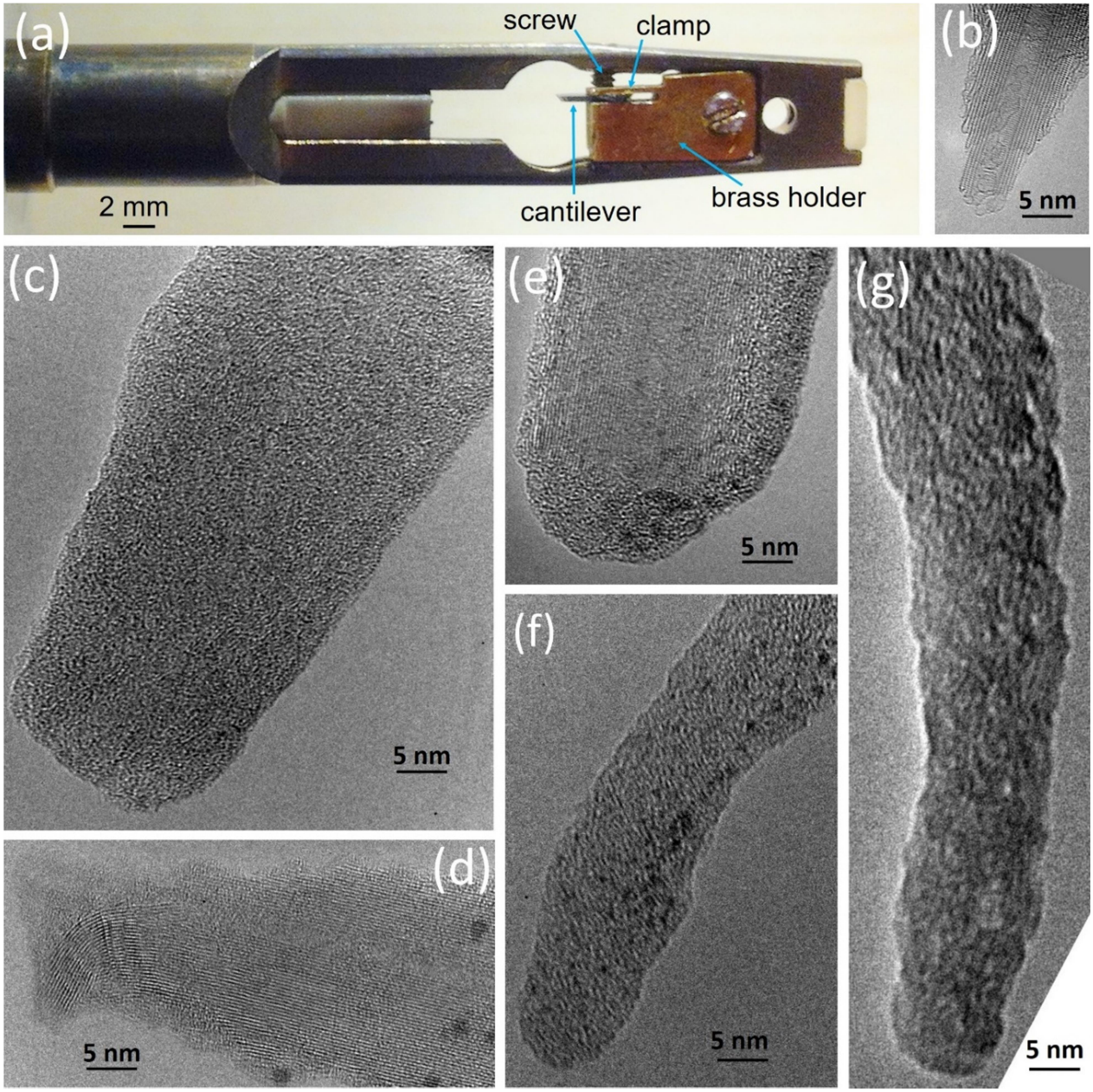

Fig. 16. (a) Detail of the modified TEM specimen holder used to investigate carbon cones when mounted as SPM probes. **(b)** HRTEM image of the apex of the as-prepared carbon cone already shown in **Fig. 15a**, for dimensional comparison with images (c) to (g) which all are at the same scale. **(c) to (f)** HRTEM images of FIBID-mounted carbon cone apices; dark spots are assumed to be gallium atoms or clusters, or

possibly nanoparticles from the welding material (Pt or W). **(g)** A cone apex from a gluing-mounted CnC probe. Images in (b) to (e) were taken with a FEI Titan Cube operated at 80 kV. Images in (f) and (g) were taken with a FEI Tecnai operated at 100kV.

An important statement is that, in spite of the relatively low TEM electron beam energy (80 keV for the images provided as Figs. 16c-e, and 100 keV for the images given as Figs. 16f-g), the carbon material from the CnC probe tips (either FIBID-mounted or gluing-mounted) was quite sensitive to the electron beam and amorphized rapidly. It was then impossible to determine which extent of the amorphization was due to the mounting process and to the TEM observation, respectively. This high sensitivity of the carbon cones, especially at their apex, to electron irradiation in the energy range used (80 or 100 keV) during our TEM investigation was unexpected, as it is atypical for carbon nano-objects with very similar texture and nanotexture such as arc-prepared concentric multi-wall CNTs (MWCNTs), and even for single-wall CNTs (SWCNTs). For instance, an electron energy threshold of 86 keV was calculated for a safe TEM investigation of SWCNTs [41], although they are even more sensitive to electron irradiation than MWCNTs [42]. The reason for this behavior discrepancy between CNTs and carbon cones is likely to relate to the occurrence of a high number of specific defects affecting the graphenes in the cones such as free graphene-edges and other defective terminations such as "loops" and "zips" [23] (Figs. 4 and 15) which do not exist in SWCNTs and arc-prepared concentric MWCNTs. Generally speaking, defective carbon lattices have been shown to exhibit an increased structural sensitivity to irradiation in the literature. This was observed for instance in SWCNTs increasingly altered by chemical treatments [43], and for carbon lattices involving undercoordinated carbon atoms [44]. This might explain why cones previously damaged by FIBID steps cannot withstand a TEM 80 keV electron beam (Figs. 16c-e) without altering further, whereas cones not previously subjected to any electron or ion beam are able to withstand the impact of a TEM electron beam of 80 keV (Fig. 15) but not of 100 keV (Fig. 16g).

A consequence of the observations above is that the TEM technique appears to be useless for assessing the extent of damages brought by the irradiation episodes during the mounting processes because it is itself destructive, even when operated at voltages in the range 80-100 kV, *i.e.*, around the limit or below the energy needed to promote C-C bond breaking and knock-on atom displacements [40-42]. Carrying out quality control of the probe apices before use would only make sense by using HRTEM with electron beam energy not higher than 80 keV.

Generally speaking, the observations and related comments reported in current Section 5 point out the need to check the structural state of the carbon probes when they are prepared by means of processes involving etching mechanisms, *e.g.*, plasma [20] and electrochemistry [21].

6. Preliminary test of the suitability of CnC probes for AFM

Examples of AFM images from preliminary tests aiming at verifying the suitability of CnC as probes for SPM are provided in Fig. 17. A series of samples with different topographies was chosen to assess the performances of CnC probes over a wide range of roughness values, from sub-nanometric to hundreds of nanometers. The tapping mode was used in all cases.

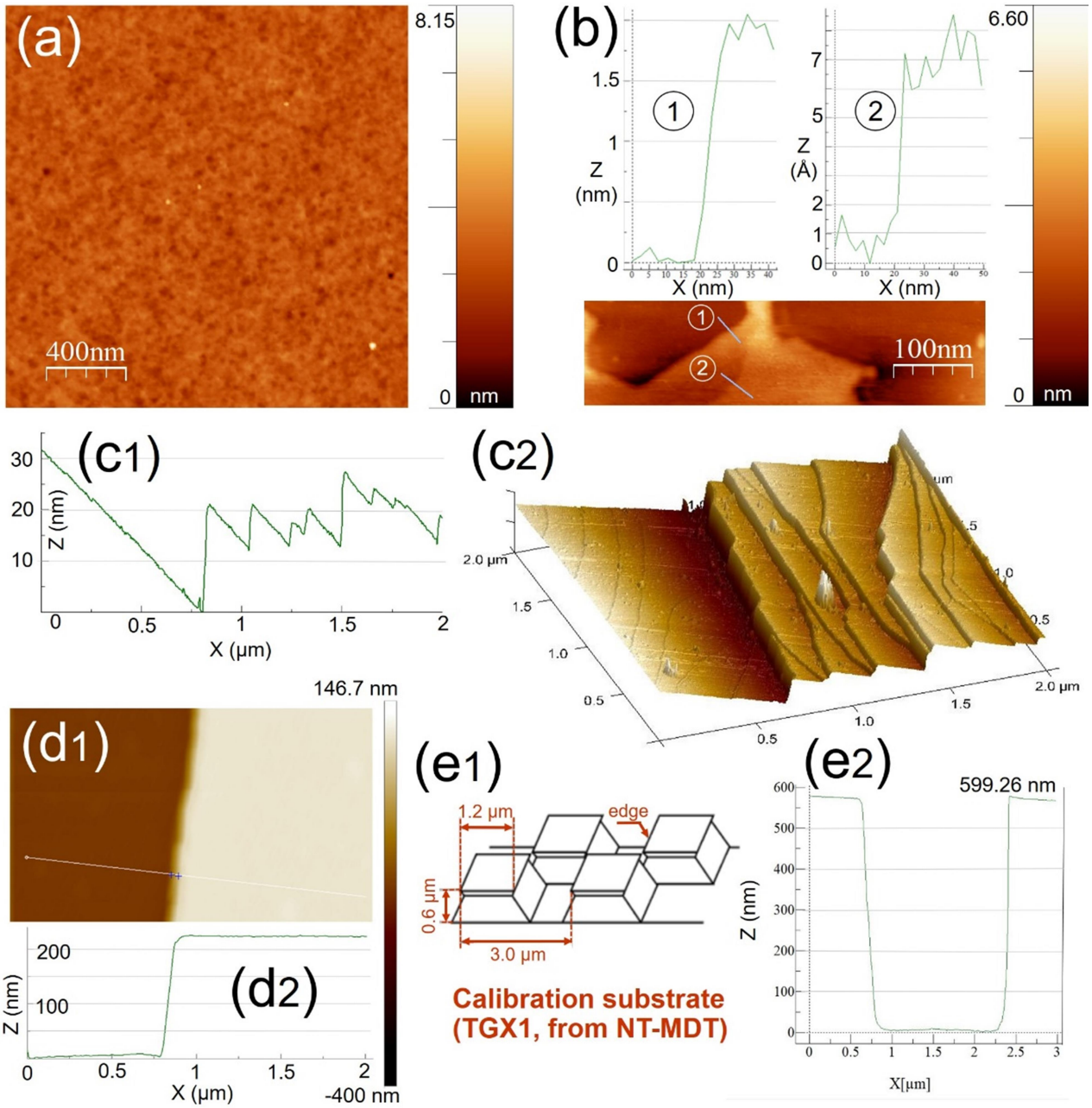

Fig. 17. AFM topography images and profiles (except **e1** - sketch) of various substrates. **(a)** Regular Si wafer surface, obtained with a FEBID-welded CnC-probe. **(b)** HOPG surface, obtained with a FIBID-welded CnC-probe. **(c)** Structured Si surface. **(d)** Standard Si surface calibration substrate with a step. **(e)** TGX1 calibration substrate. Images from (c) to (e) were obtained with glued-type CnC-probes. All AFM images and profiles were obtained using a Nanoscope IIIa AFM from Bruker.

Fig. 17a shows a regular aspect of a Si/SiO_2 wafer surface. The image exhibits a very good lateral resolution as evidenced on the four nanosized impurities which appear as white dots. The rms roughness of the image is 0.36 nm, which is in the expected range for such a surface.

Fig. 17b shows two steps from a HOPG substrate (Bruker), one (step #1) with a height of ~2 nm, the other (step #2) in the range of 0.6-0.7 nm. Considering that a graphene is 0.34 nm thick [36], the steps may correspond to stacks of 6 and 2 graphenes, respectively. However, the literature has shown that the thickness value determined by tapping mode AFM can be largely influenced by the operating parameters [45], as well as by the presence of a water film [46,47] although this may depend on the type of substrate. Therefore, the number of graphenes here given should only be considered tentative. Tentatively refining the measurement, for instance by using peak-force AFM along with specific high force setpoint [47], would have been possible, but it is out of scope here, as the purpose of Fig. 17 is merely to provide examples and a proof of concept. It is worth noting that the CnC probe used in the case of Fig. 17b was welded by FIBID. Therefore, despite the broadening of the cone apex resulting from the ion-irradiation damages makes them poorly suitable when lateral resolution is needed, such probes may still be used for substrates with limited topography variations.

Figs. 17c1-c2 provide a 3D topography image of a Si surface structured with a variety of steps with various heights (c2), along with a related topography profile across the steps over a length of 2 µm (c1). The CnC probe resolves nicely both the steps with sub-nanometer height and large ones as high as 20 nm.

Figs. 17d1-d2 illustrate a step with a 200 nm-high vertical rise of a standard calibration Si substrate (d1). The related profile obtained across the step (d2) shows an offset with respect to verticality (angle 71° +/- 1°) which reveals the aspect ratio of the CnC probe.

Figs. 17e1-e2 illustrate the topography of a TGX1 calibration substrate (from NT-MDT) and its dimensional characteristics (e1), and provides a typical topography profile of one of the depressions between two square plots (e2). The inverse top-hat shape of the profile illustrates the high aspect ratio of the CnC probe. The slight dissymmetry between the left and right "vertical" parts originates from the equipment, not from a misalignment of the CnC with respect to the cantilever axis. The bottom of the depression is well seen over its whole length in spite of the large depth (600 nm). This last example shows that the structure and rigidity of the CnC probes allow imaging samples with very large rugosity.

A whole campaign of investigations comparing CnC probes and standard Si-probes, and eventually CNT probes, for a variety of SPM modes including non-conducting (AFM, peak-force quantitative nano-mechanical AFM) and conducting ones (conducting AFM, Kelvin force

microscopy) was carried out. The related results will be disclosed in a series of forthcoming dedicated papers, which will demonstrate that CnC probes, among other benefits, are more versatile than Si probes and can be used as genuine multimode SPM probes.

7. Conclusions

New carbon probes for scanning probe microscopy (SPM) were introduced, based on unique all-graphenic cone-bearing carbon micro-objects (CnC). Among the various procedures investigated for mounting a CnC onto a doped-Si cantilever support, the most cost-efficient one was to glue it with a UV-curable single-component resin using a micromanipulator under an optical microscope. A specific drawback of this technique, however, is that the resin is not electrically conductive, making the CnC probe unsuitable for conducting SPM modes. This problem will be fixed as soon as a conductive glue will be available, for instance by adding conducting nanoparticles, preferably as elongated nanorods instead of round grains so that to favor the percolation at lower loading rate. Indeed, conducting glues on the market involve conducting microsized components (*e.g.*, silver flakes) which are definitely non-suitable for fixing objects the dimensions of which are smaller.

Welding the CnC with W (preferably than Pt) was explored as a possible alternative for providing CnC probes conductive enough for being suitable for conducting SPM modes. However, any process involving ion beam-related steps (such as FIB-etching or FIBID) has to be discarded, because of the severe structural damages brought to the carbon structure. Such a statement is general, and makes a warning regarding any ion-beam-based microtechnology process involving carbon objects for which maintaining their textural and nanotextural integrity is essential.

A compromise can be to use a FEBID process to produce CnC probes of an acceptable quality suitable for both conducting and non-conducting SPM modes. However, this comes with several specific drawbacks, *i.e.*, processing times ~8 times longer than the gluing technique, probe surface amorphization, and risk for loose CnC attachment.

Similar to ion irradiation but in a much lesser extent, an unexpected sensitivity of carbon cones to electron irradiation in TEM was revealed, making them damaged even under electron irradiation conditions (100 keV) which usually do not significantly affect structurally-close graphene-based nano-objects such as CNTs. This sensitivity is attributed to the high number of structural defects related to graphene terminations specific to the carbon cones with respect to CNTs, namely free graphene-edges (hence, under-coordinated carbon atoms), and highly

constrained graphene terminations, as both certainly increase significantly the energy of the system.

This first generation of CnC probes reported here suffers from the frequent misalignment of the cone axis versus the CnC axis in the as-grown state itself. Further work is needed in this regard, and the problem will be dramatically reduced by growing the carbon cones onto straight and perfectly aligned carbon nanotubes (instead of randomly-grown CNTs as it is so far). It is expected that such an achievement should also allow a much better control of the alignment to be achieved during the mounting process.

The morphological, structural, textural, and nanotextural characteristics of the cones strongly suggest that their performances as SPM probes could overpass that of the current Si probes on market regarding, *e.g.*, resolution, reactivity to surrounding conditions (humidity, for instance, thanks to the hydrophobicity of carbon), wear resistance, durability, and SPM mode versatility. More specifically, CnC probes are expected to be much less fragile than sp^3-C-based (diamond) probe, and less flexible than CNT-based probes. In addition, the chemical nature of the cones (graphenic carbon) provides access to organic chemistry processes for tailoring the probe tip with a variety of chemical groups at will, for instance for use as probes for chemical force microscopy. Many of these aspects were actually investigated already, demonstrating the superior performances of CnC probes over standard Si-probe (and eventually CNT probes) in several instances. The results will be published in forthcoming articles. As a large variety of SPM modes were tested (atomic force microscopy (AFM), peak-force quantitative nanomechanical AFM, conducting AFM, Kelvin force microscopy), one of the valuable benefits of CnC probes appears to be their versatility, which allows considering them as multimode SPM probes.

Declaration of Competing Interest

The authors declare that they have no known competing financial interests or personal relationships that could have appeared to influence the work reported in this paper.

Acknowledgments

This study has been supported through the EUR grant NanoX n°ANR-17-EURE-0009 in the framework of the "Programme des Investissements d'Avenir", the ANR project CANAC (ANR-12-EMMA-0044-01), the Government of Aragon (project DGA E13-20R), the Spanish MICINN (PID2019-104739GB-100/AEI/10.13039/501100011033), the European Union H2020 programs "ESTEEM3" (Grant number 823717). The Pontificia Universidad Católica Madre y Maestra

(Santiago, Dominican Republic) is also thanked for providing the grant for G. P.. M. Kandara and A. C. Torres-Dias are thanked for performing some of the SEM images, M. Delmas (CEMES) for providing the SEM images as Figs. 2b-d, R. Wang (CEMES-INA) for providing images as Figs. 4 and 15, S. Joulié for operating the FEI Tecnai TEM at CEMES. The HRTEM work with a FEI Titan Cube was conducted at the *Laboratorio de Microscopias Avanzadas* (LMA), Universidad de Zaragoza, Spain.

Supplementary materials

Supplementary material associated with this article can be found, in the online version, at

References

[1] P. Eaton, P. West, Atomic Force Microscopy, *(*Hbk) Oxford University Press, 2010.
[2] B. Bhushan, O. Marti, Scanning probe microscopy - Principle of operation, instrumentation, and probes, in: B. Bhushan (ed.), Handbook of Nanotechnology, Chapter 21, Springer-Verlag, Heidelberg, Germany, 2010, pp.573-617.
[3] A. Noy, D.V. Vezenov, C.M. Lieber, Chemical force microscopy, Annu. Rev. Mater. Sci. 27 (1997) 381-421.
[4] C.V. Nguyen, Q. Ye, M. Meyyappan, Carbon nanotube tips for scanning probe microscopy: fabrication and high aspect ratio nanometrology, Sci. Technol. 16 (2005) 2138-2146.
[5] L. Guo, R. Wang, H. Xu, J. Liang Wear-resistance comparison of carbon nanotubes and conventional silicon-probes for atomic force microscopy, Wear 258 (2005) 1836–1839.
[6] H. Dai, J.H. Hafner, A.G. Rinzler, D.T. Colbert, R. Smalley, Nanotubes as nanoprobes in scanning probe microscopy, Nature 384 (1996) 147-150.
[7] Q. Ye, A.M. Cassell, H. Liu, K.-J. Chao, J. Han, M. Meyyappan, Large-scale fabrication of carbon nanotube probe tips for atomic force microscopy critical dimension imaging applications, Nano Lett. 4 (2004) 1301-1308.
[8] S. Marsaudon, C. Bernard, D. Dietzel, C.V. Nguyen, A.-M. Bonnot, J.-P. Aimé, R. Boisgard, Carbon nanotubes as SPM tips: mechanical properties of nanotube tips and imaging, in: B. Bhushan, H. Fuchs, M. Tomitori (eds.), Applied Scanning Probe Methods VIII, Nano Science and Technology, Springer, Berlin, Heidelberg, 2008.
[9] N. Wilson, J.V. Macpherson, Carbon nanotube tips for atomic force microscopy, Nature Nanotechnol. 4 (2009) 483-491.
[10] R.M. Stevens, New carbon nanotube AFM probe technology, Mater. Today 12 (2009) 42-45.
[11] M.M.J. Treacy, TW. Ebbesen, J.M. Gibson, Exceptionally high Young's modulus observed for individual carbon nanotubes, Nature 381 (1996) 678-680.
[12] E.W. Wong, P.E. Sheehan, C.M. Lieber, Nanobeam mechanics: elasticity, strength, and toughness of nanorods and nanotubes, Science 277 (1997) 1971-1975.
[13] T. Hantschel, M. Tsigkourakos, L. Zha, T. Nuytten, K. Paredis, B. Majeed, W. Vandervorst, Diamond scanning probes with sub-nanometer resolution for advanced nanoelectronics device characterization, Microelectron. Eng. 159 (2016) 46–50.
[14] J. Martinez, T.D. Yuzvinsky, A.M. Fennimore, A. Zettl, R. Garcia, C. Bustamante, Length control and sharpening of atomic force microscope carbon nanotube tips assisted by an electron beam, Nanotechnol. 16 (2005) 2493–2496.

[15] M.C. Strus, A. Raman, C.-S. Han, C.V. Nguyen, Imaging artefacts in atomic force microscopy with carbon nanotube tips, Nanotechnology 16 (2005) 2482-2492.
[16] X. Hu, H. Wei, Y. Deng, X. Chi, J. Liu, J. Yue, Z. Peng, J. Cai, P. Jiang, L. Sun, Amplitude response of conical multiwalled carbon nanotube probes for atomic force microscopy, Roy. Soc. Chem. Adv. 9 (2019) 429-434.
[17] H. Allouche, M. Monthioux, R. Jacobsen, Chemical vapor deposition of pyrolytic carbon on carbon nanotubes: (I) synthesis and morphology, Carbon 41 (2003) 2897-2912.
[18] G. Paredes, G. Seine, R. Cours, F. Houdellier, H. Allouche, T. Ondarçuhu, F. Piazza, M. Monthioux, Synthesis and (some) applications of carbon-nanotube-supported pyrolytic carbon nanocones, Ind. J. Eng. Mater. Sci. 27 (2020) 1091-1094.
[19] G. Paredes, Development of New Probes Based on Carbon Nanocones for Near-Field Microscopies. PhD Thesis, University of Toulouse 3, France, October 28, 2020.
[20] I.-C. Chen, L.-H. Chen, X.-R. Ye, C. Daraio, S. Jin, C.A. Orme, A. Quist, R. Lal, Extremely sharp carbon nanocone probes for atomic force microscopy imaging, Appl. Phys. Lett. 88 (2006) 153102.
[21] J. Sripirom, S. Noor, U. Kölher, A. Schulte, Easily made and handled carbon nanocones for scanning tunneling microscopy and electroanalysis, Carbon 49 (2011) 2402-2412.
[22] H. Allouche, M. Monthioux, Chemical vapor deposition of pyrolytic carbon on carbon nanotubes. Part II: Texture and structure. Carbon 43 (2005) 1265-1278.
[23] G. Paredes, R. Wang, P. Puech, G. Seine, J.-M. Leyssale, R. Arenal, A. Masseboeuf, F. Piazza, M. Monthioux, Texture, nanotexture, and structure of carbon nanotube-supported carbon cones, ACS nano 16 (2022) 9287-9296.
[24] M. Monthioux, H. Allouche, R. Jacobsen, Chemical vapor deposition of pyrolytic carbon on carbon nanotubes. Part III: Formation mechanisms, Carbon 44 (2006) 3183-3194.
[25] G. Paredes, T. Ondarçuhu, M. Monthioux, F. Piazza, Unveiling the existence and role of a liquid phase in a high temperature (1400 °C) pyrolytic carbon deposition process, Carbon Trends 5 (2021) 10017.
[26] M. Berd, P. Puech, A. Righi, A. Benfdila, M. Monthioux, Resonant laser-induced formation of double-walled carbon nanotubes from peapods under ambient conditions, Small 8 (2012) 2045–2052.
[27] S. Mamishin, Y. Kubo, R. Cours, M. Monthioux, F. Houdellier, 200 kV cold field emission source using carbon cone nanotip: application to scanning transmission electron microscopy. Ultramicroscopy 182 (2107) 303-307.
[28] J.M. De Teresa, R. Córdoba, A. Fernández-Pacheco, S. Sangiao, M.R. Ibarra, Nanoscale electrical contacts grown by focused ion beam (FIB)-induced deposition, in: Z.M. Wang (ed.), FIB Nanostructures, Chapter 5, Lecture Notes in Nanoscale Science and Technology Series, vol.20, Springer International Publishing, Switzerland, 2013, pp.95-122.
[29] F. Houdellier, A. Masseboeuf, M. Monthioux, M.J. Hÿtch, New carbon cone nanotip for use in a highly coherent cold field emission electron microscope, Carbon 50 (2012) 2037-2044.
[30] A.D. Slattery, A.J. Blanch, J.S. Quinton, C.T. Gibson, Efficient attachment of carbon nanotubes to conventional and high-frequency AFM probes enhanced by electron beam processes, Nanotechnol. 24 (2013) 235705.
[31] J.P. Cleveland, S. Manne, D. Bocek, P. K. Hansma, A nondestructive method for determining the spring constant of cantilevers for scanning force microscopy, Rev. Sci. Instr. 64 (1993) 403-405.
[32] A.D. Slattery, J.S. Quinton, C.T. Gibson, Atomic force microscope cantilever calibration using a focused ion beam, Nanotechnol. 23 (2012) 285704
[33] C. Kocabas, S.-H. Hur, A. Gaur, M.A. Meitl, M. Shim, J. A. Rogers, Guided growth of large-scale, horizontally aligned arrays of single-walled carbon nanotubes and their use in thin-film transistors, Small 1 (2005) 1110-1116.
[34] F. Tuinstra, J.L. Koenig, Raman spectrum of graphite, J. Chem. Phys. 53 (1970) 1126–1130.
[35] L.G. Cançado, M.G. Da Silva, E.H.M. Ferreira, F. Hof, K. Kampioti, K. Huang, A. Pénicaud, C.A. Achete, R.B. Capaz, A. Jorio, Disentangling contributions of point and line defects in the Raman spectra of graphene-related materials, 2D Mater. 4 (2017) 025039.

[36] J.W. Weber, V.E. Calado, M.C.M. van de Sanden, Optical constants of graphene measured by spectroscopic ellipsometry, Appl. Phys. Lett. 97 (2010) 091904.
[37] E.T. Arakawa, M.W. Williams, T. Inagaki, Optical properties of arc-evaporated carbon films between 0.6 and 3.8 eV, J. Appl. Phys. 48 (1977) 3176-3177.
[38] J.M. De Teresa, R. Córdoba, A. Fernández-Pacheco, O. Montero, P. Strichovanec, M.R. Ibarra, Origin of the difference in the resistivity of as-grown focused-ion-and focused-electron-beam-induced Pt deposit, J. Nanomater. (2009) 936863.
[39] M.S. Raghuveer, P.G. Ganesan, J. d'Arcy-Gall, G. Ramanath Nanomachining carbon nanotubes with ion beams, Appl. Phys. Lett. 84 (2004) 4484-4486.
[40] A.V. Krasheninnikov, K. Nordlund, Ion and electron irradiation-induced effects in nanostructured materials, J. Appl. Phys. 107 (2010) 0701301.
[41] B.E. Smith, D.E. Luzzi, Electron irradiation effects in single wall carbon nanotubes, J. Appl. Phys. 90 (2001) 3509-3515.
[42] F. Banhart, Irradiation effects in carbon nanostructures, Rep. Prog. Phys. 62 (1999) 1181–1221.
[43] M. Monthioux, B.W. Smith, B. Burteaux, A. Claye, J.E. Fischer, D.E. Luzzi, Sensitivity of single-wall carbon nanotubes to chemical processing: an electron microscopy investigation, Carbon 39 (2001) 1251–1272.
[44] A.V. Krasheninnikov, F. Banhart, J.X. Li, A.S. Foster, R.M. Nieminen, Stability of carbon nanotubes under electron irradiation: Role of tube diameter and chirality, Phys. Rev. B 72 (2005) 125428.
[45] P. Nemes-Incze, Z. Osvath, K. Kamaras, L.P. Biro, Anomalies in thickness measurements of graphene and few layer graphite crystals by tapping mode atomic force microscopy, Carbon 46 (2008) 1435-1442.
[46] H. Lee, J.Y. Park Height determination of single-layer graphene on mica at controlled humidity using atomic force microscopy, Rev. Sci. Instrum. 90 (2019) 103702.
[47] C.J. Shearer, A.D. Slattery, A.J. Stapleton, J.G. Shapter, C.T. Gibson, Accurate thickness measurement of graphene, Nanotechnol. 27 (2016) 125704.

New probes based on carbon nano-cones for scanning probe microscopies

Robin Cours[a], Germercy Paredes[a,b,†], Aurélien Masseboeuf[a], Thierry Ondarçuhu[a,c], Grégory Seine[a], Pascal Puech[a], Raul Arenal[d,e,f], Fabrice Piazza[b], Marc Monthioux[a]

Supplementary Information

Details on Calculation-1 regarding the weight of a CnC object based on its nature and dimensions

In order to estimate the weight of a typical microsized carbon object (CnC) as those used in this work and shown in Figures 3, 6, 7, 9, 11, 12 and 13 of the main paper, we considered a model object consisting of a central cylindric part added with two cones, with the following dimensions:

Cylinder:

Length L_f = 15 µm

Radius r_f = 1 µm

→ Volume $V_f = \pi \times r_f^2 \times L_f = 3.14 \times (1 \times 10^{-6})^2 \times (15 \times 10^{-6}) = 47.1 \times 10^{-18}$ m^3

The graphenes making this part of the object exhibit a good-grade nanotexture (*i.e.*, they are barely distorted) but with short L_a of few nm [1]. The overall texture is porous (few-nanometer-wide pores), which generates the rough surface [1], and makes it similar to a carbon obtained from non-graphitizable precursor such as glassy carbon. We therefore considered the density similar to that of a glassy carbon, *i.e.*, ρ_f = 1400 kg/m^3 [2].

→ Weight P_f of the cylinder part: $\rho_f \times V_f = 1400 \times 47 \times 10^{-18} = 6.58 \times 10^{-14}$ kg (65.8 pg).

Cone:

Length L_c = 5 µm

Radius r_c = 0.4 µm

→ Volume $V_c = (\pi \times r_c^2 \times L_c) / 3 = 3.14 \times (0.4 \times 10^{-6})^2 \times (5 \times 10^{-6}) / 3 = 0.84 \times 10^{-18}$ m^3

The graphenes making the cones are perfect (high-grade nanotexture) and well-packed, generating a dense, pore-free texture (regardless of the inner cavity of the central CNT) similar to that of genuine graphite (see [3] and Figure 4 in the main paper). The intergraphene distance, however, is

† Corresponding Authors.
E-mail addresses: gd.paredes@ce.pucmm.edu.do (G. Paredes); marc.monthioux@cemes.fr (M. Monthioux)

larger (0.34 nm) than that in genuine graphite (0.33 nm) because of the turbostratic stacking induced by the concentric display of the graphenes, which prevents the superimposed lattices to ideally match. We therefore considered the density slightly lower than that of genuine graphite, *i.e.*, $\rho_c = 2000$ kg/m^3.

→ Weight P_c of a cone: $\rho_c \times V_c = 2000 \times 0.84 \times 10^{-18} = 1680 \times 10^{-18} = \sim 0.17 \times 10^{-14}$ kg (1.7 pg)

Therefore, the weight of a typical CnC is: $P_f + (2 \times P_c) = 65.8 + (2 \times 1.7) =$ **~69 pg**

Details on Calculation-2 regarding the weight of a CnC object based on the resonance frequency downshift of the cantilever

The nominal resonance frequency f of the cantilever used in Figure 10a was 157×10^3 Hz. This corresponds to a Type2 cantilever, the spring constant k of which is ~2.5 kg/m (or 25 N/m, as written in Table 1 of the main paper).

After a CnC is mounted at the tip of the cantilever, the resonance frequency exhibits a downshift $\Delta f = 2 \times 10^3$ Hz.

There is a relation between the oscillation frequency of a spring positioned vertically and the mass attached to it through the spring constant k. It is admitted to extrapolate this relation to the case of an oscillating cantilever of mass m. However, as opposed to the case of a spring, a cantilever is horizontal and its oscillation is only maximum at its tip. Therefore, a correcting factor has to be applied to the mass m so that to obtain a kind of "spring-equivalent" mass called the "effective mass" m_{eff}. On the other hand, a CnC added to the cantilever tip corresponds to an additional mass Δm which does not require a correcting factor to be applied since actually added to the tip only [4]. However, calculating m_{eff} is not necessary here, as Δm, f, and k are related by the following equation [4]:

$$\Delta m = k \times (1/f_m^2 - 1/f_0^2) / (2\pi)^2$$

where f_0 is the initial resonance frequency of the cantilever, and f_m is the resonance frequency of the cantilever after the mass Δm (the CnC) is added.

$$\Delta m = 2.5 \times [1/(157 \times 10^3)^2 - 1/(155 \times 10^3)^2] / (2 \times 3.14)^2 = -6.67 \times 10^{-14} \text{ kg (}\sim\textbf{67 pg)}$$

Therefore, because the agreement between the result from Calculation-1 (69 pg) and that from Calculation-2 (67 pg) is fairly good, it can be said that the 2 kHz downshift of the resonance frequency of the cantilever is significant and induced by the added weight of a CnC object to the cantilever tip.

References

[48] Allouche H., Monthioux M. *Chemical vapor deposition of pyrolytic carbon on carbon nanotubes. Part II: Texture and structure*. **Carbon** 43 (2005) 1265-1278.

[49] Craievich A. F. *On the structure of glassy carbon*. **Mater. Res. Bull.** 11 (1976) 1249-1255.

[50] Paredes G., Wang R., Puech P., Seine G., Leyssale J.-M., Arenal R., Masseboeuf A., Piazza F. Monthioux M. *Texture, nanotexture, and structure of carbon nanotube-supported carbon cones*. **ACS nano** 16 (2022) 9287-9296.

[51] Cleveland J. P., Manne S., Bocek D., Hansma P. K. *A nondestructive method for determining the spring constant of cantilevers for scanning force microscopy*. **Rev. Sci. Instr.** 64 (1993) 403-405.